Comput. Methods Appl. Mech. Engrg. 213–216 (2012) 104–112

Contents lists available at SciVerse ScienceDirect

Comput. Methods Appl. Mech. Engrg.

journal homepage: www.elsevier.com/locate/cma

Isogeometric analysis and domain decomposition methods

Christian Hesch *, Peter Betsch

Department of Mechanical Engineering, University of Siegen, Germany

ARTICLE INFO

Article history:
Received 12 June 2011
Received in revised form 5 December 2011
Accepted 10 December 2011
Available online 29 December 2011

Keywords:
Isogeometric analysis
NURBS
Domain decomposition
Mortar energy-momentum
Nonlinear elasticity

ABSTRACT

In the present work we use the mortar finite element method for the coupling of nonconforming discretized sub-domains in the framework of nonlinear elasticity. The mortar method has been shown to preserve optimal convergence rates (see Laursen (2002) [25] for details) and is variationally consistent. We show that the method can be applied to isogeometric analysis with little effort, once the framework of NURBS based shape functions has been implemented. Furthermore, a specific coordinate augmentation technique allows the design of an energy–momentum scheme for the constrained mechanical system under consideration. The excellent performance of the redesigned mortar method as well as the energy–momentum scheme is illustrated in representative numerical examples.

1. Introduction

Several decades ago, Lagrangian shape functions have been established as preferred basis for the numerical approximation of partial differential equations by means of the finite element method. In contrast, NURBS based shape functions, emanating from the field of Computer Aided Design (CAD), have been established as a vitally important tool for designers. Isogeometric analysis (see [23,8]) has been developed to link both worlds, using NURBS as a basis for Galerkin-based discretization schemes.

For the past few years, a wide range of problems have been addressed in the framework of isogeometric analysis, demonstrating the advantages of this approach. Isogeometric analysis has been applied to the field of fluid mechanics [2], structural analysis [9,10,28], shell formulations [3], phase field models [13] and contact problems [33,29]. For a comprehensive survey see Cottrell et al. [7].

In this work, we apply domain decomposition methods to isogeometric analysis. These methods allow to subdivide bodies into several sub-domains, which can be meshed independently, using either Lagrangian or NURBS based shape functions. Additionally, h-, p- or k-refinement methods can be applied to single sub-domains with no regard to other sub-domains. In particular, we use mortar finite element mesh tying methods to join the dissimilarly meshed regions. Originally developed in Bernadi et al. [4], several enhancements have been developed during the past years (see [34,35,12,31]). Furthermore, highly advanced techniques in the context of iterative solvers have been developed in recent years (see lecture notes in [1]).

Numerical time integration schemes that facilitate algorithmic conservation of total energy as well as the momentum maps are of major importance for a wide range of applications, where the lack of algorithmic energy conservation can cause numerical blow-up behavior. In fact, energy–momentum conserving time-stepping schemes provide enhanced numerical stability in the field of nonlinear structural- and thermoelastic dynamics (cf. [14,5,19,24]). They have been applied successfully to contact [26,6,27,15,17,21,20] as well as to domain decomposition problems [18].

An outline of the present work is as follows. A summary of the basic equations in the context of continuum mechanics is given in Section 2. In particular, we derive the strong and the weak form of the problem. In Section 3 we apply the spatial discretization using NURBS based shape functions and derive a redesigned mortar method based on the discrete virtual work. To this end, we verify frame-indifference properties of the modified constraints. The equations of motion and the energy–momentum scheme are dealt with in Section 4. Representative numerical examples are presented in Section 5. Eventually, conclusions are drawn in Section 6.

2. Formulation of the problem

In this section we provide a short outline of the fundamental equations. We consider a general non-linear mechanical system, artificially subdivided into several sub-domains i,[1] occupying the space $\mathcal{B}_0^{(i)} \subset \mathbb{R}^3$ in the reference configuration. The deformation map-

* Corresponding author. Tel.: +49 271 740 2101; fax: +49 271 740 2436.
E-mail address: christian.hesch@uni-siegen.de (C. Hesch).

[1] Without loss of generality we restrict ourself to a two body problem, i.e. $i \in \{1,2\}$.

0045-7825/$ - see front matter © 2011 Elsevier B.V. All rights reserved.
doi:10.1016/j.cma.2011.12.003

ping $\boldsymbol{\varphi}^{(i)}(\boldsymbol{X}^{(i)},t):\mathcal{B}_0\times[0,T]\to\mathbb{R}^3$, where [0,T] denotes the time interval under consideration, characterizes the current position of the material point $\boldsymbol{X}^{(i)}\in\mathcal{B}_0^{(i)}$ at time t. The linear momentum is given by $\boldsymbol{\pi}=\rho_0\boldsymbol{v}$, where ρ_0 denotes the density in the reference configuration and $\boldsymbol{v}:\mathcal{B}_0\times[0,T]\to\mathbb{R}^3,\ \boldsymbol{v}=\dot{\boldsymbol{\varphi}}=\partial\boldsymbol{\varphi}/\partial t$ the material velocity. The material surfaces $\partial\mathcal{B}_0^{(i)}$ are partitioned into the Dirichlet boundary $\Gamma_u^{(i)}$, the Neumann boundary $\Gamma_\sigma^{(i)}$ and the internal interface $\Gamma_d^{(i)}$ between the sub-domains. We require that the three portions $\Gamma_u^{(i)},\Gamma_\sigma^{(i)}$ and $\Gamma_d^{(i)}$ satisfy

$$\Gamma_u^{(i)}\cup\Gamma_\sigma^{(i)}\cup\Gamma_d^{(i)}=\partial\mathcal{B}_0^{(i)} \tag{1}$$

and

$$\Gamma_u^{(i)}\cap\Gamma_\sigma^{(i)}\cap\Gamma_d^{(i)}=\emptyset, \tag{2}$$

on each sub-domain. Furthermore, we assume the existence of a strain energy function $\Psi(\boldsymbol{C}^{(i)}):\mathcal{B}_0^{(i)}\times[0,T]\to\mathbb{R}$, where $\boldsymbol{C}^{(i)}:\mathcal{B}_0^{(i)}\times[0,T]\to\mathbb{R}^{3\times3}$ denotes the right Cauchy-Green deformation tensor, given by $\boldsymbol{C}^{(i)}=\boldsymbol{F}^{(i),T}\boldsymbol{F}^{(i)}$ and $\boldsymbol{F}^{(i)}:\mathcal{B}_0^{(i)}\times[0,T]\to\mathbb{R}^{3\times3},\boldsymbol{F}^{(i)}=D\boldsymbol{\varphi}^{(i)}$ denotes the deformation gradient. The Lagrangian form of the balance of linear momentum is given by

$$\begin{aligned}\dot{\boldsymbol{\varphi}}^{(i)}&=\rho_0^{-1}\boldsymbol{\pi}^{(i)},\\ \dot{\boldsymbol{\pi}}^{(i)}&=\mathrm{Div}(\boldsymbol{P}^{(i)})+\boldsymbol{B}^{(i)},\end{aligned} \tag{3}$$

supplemented by the boundary conditions

$$\begin{aligned}\boldsymbol{\varphi}^{(i)}&=\bar{\boldsymbol{\varphi}}^{(i)}\quad\text{on }\Gamma_u^{(i)}\times[0,T],\\ \boldsymbol{P}^{(i)}\boldsymbol{N}^{(i)}&=\bar{\boldsymbol{T}}^{(i)}\quad\text{on }\Gamma_\sigma^{(i)}\times[0,T],\end{aligned} \tag{4}$$

where $\boldsymbol{P}=2\boldsymbol{F}\nabla_C\Psi(C)$ denotes the first Piola–Kirchhoff stress tensor, $\boldsymbol{N}^{(i)}$ the outward unit normal vector in the reference configuration of body $i,\boldsymbol{B}^{(i)}$ the applied body forces and $\bar{\boldsymbol{T}}^{(i)}$ the prescribed tractions. To define the interface conditions on $\Gamma_d^{(i)}$ we introduce a pseudo-traction vector $\boldsymbol{t}^{(i)}$, defined in terms of force per unit undeformed area. To fulfill the balance of linear momentum across the interface, we require $\boldsymbol{t}^{(1)}=\boldsymbol{t}^{(2)}$ on $\Gamma_{\boldsymbol{d}^{(i)}}\times[0,T]$. Eq. (3) represents the strong formulation of the problem, whereas the weak formulation reads

$$G(\boldsymbol{\varphi},\delta\boldsymbol{\varphi})=\sum_i G^{(i)}(\boldsymbol{\varphi},\delta\boldsymbol{\varphi})=0, \tag{5}$$

where $\delta\varphi$ are admissible test functions. Setting the L_2-inner product on $\mathcal{B}_0^{(i)}$ in the usual fashion

$$\int_{\mathcal{B}_0^{(i)}}(\bullet)\cdot(\bullet)dV^{(i)}=:\langle\bullet,\bullet\rangle^{(i)}\quad\text{and}\quad\int_{\partial\mathcal{B}_0^{(i)}}(\bullet)\cdot(\bullet)d\Gamma^{(i)}=:\langle\bullet,\bullet\rangle_{\Gamma^{(i)}} \tag{6}$$

the contribution of each sub-domain i to the virtual work takes the form

$$\begin{aligned}G^{(i)}(\varphi,\delta\varphi)=&\langle\rho_R\ddot{\varphi},\delta\varphi\rangle^{(i)}+\langle\mathbf{P},\nabla_X(\delta\varphi)\rangle^{(i)}-\langle\rho_R\bar{\mathbf{B}},\delta\varphi\rangle^{(i)}\\&-\langle\bar{\mathbf{T}},\delta\varphi\rangle_{\Gamma_\sigma^{(i)}}-\langle\mathbf{t},\delta\varphi\rangle_{\Gamma_d^{(i)}},\end{aligned} \tag{7}$$

where $\langle\mathbf{t},\delta\varphi\rangle_{\Gamma_d^{(i)}}$ denotes the virtual work contributions of the coupling tractions. Additionally, we require that the balance of linear momentum across the interface

$$\sum_j-\langle\mathbf{t},\delta\varphi\rangle_{\Gamma_d^{(i)}}=\langle\mathbf{t}^{(1)},(\delta\varphi^{(1)}-\delta\varphi^{(2)})\rangle_{\Gamma_d^{(1)}}=0, \tag{8}$$

has to hold at all times $t\in[0,T]$.

3. Spatial discretization

Inspired by developments in the context of isogeometric analysis (see Cottrell et al. [7] and the references therein for a comprehensive survey of this topic) we apply NURBS based shape functions for the approximation of displacement based finite elements in space

$$\varphi^{(i),\mathrm{h}}=\sum_{A\in\omega^{(i)}}R^{A,(i)}\mathbf{q}_A^{(i)},\quad\delta\varphi^{(i),\mathrm{h}}=\sum_{A\in\omega^{(i)}}R^{A,(i)}\delta\mathbf{q}_A^{(i)}, \tag{9}$$

where

$$R^{A,(i)}=R^{\mathrm{i,j,\mathfrak{k}}}_{p,q,r}(\boldsymbol{\xi})=\frac{N_{\mathrm{i},p}(\xi)M_{\mathrm{j},q}(\eta)L_{\mathfrak{k},r}(\zeta)w_{i,j,k}}{\sum_{\hat{\mathrm{i}}=1}^{n}\sum_{\hat{\mathrm{j}}=1}^{m}\sum_{\hat{\mathfrak{k}}=1}^{l}N_{\hat{\mathrm{i}},p}(\xi)M_{\hat{\mathrm{j}},q}(\eta)L_{\hat{\mathfrak{k}},r}(\zeta)w_{\hat{\mathrm{i}},\hat{\mathrm{j}},\hat{\mathfrak{k}}}}. \tag{10}$$

Here, p, q, r denotes the order of the non-rational B-Spline shape functions N, M and L, recursively defined as follows

$$N_{\mathrm{i},p}=\frac{\xi-\xi_{\mathrm{i}}}{\xi_{\mathrm{i}+p}-\xi_{\mathrm{i}}}N_{\mathrm{i},p-1}(\xi)+\frac{\xi_{\mathrm{i}+p+1}-\xi}{\xi_{\mathrm{i}+p+1}-\xi_{\mathrm{i}+1}}N_{\mathrm{i}+1,p+1}(\xi), \tag{11}$$

beginning with

$$N_{\mathrm{i},0}(\xi)=\begin{cases}1 & \text{if }\xi_{\mathrm{i}}\leqslant\xi<\xi_{\mathrm{i}+1},\\ 0 & \text{otherwise.}\end{cases} \tag{12}$$

The definition for M and L follows analogously. Furthermore, $w_{\mathrm{i,j,\mathfrak{k}}}$ are NURBS weights, for details see Piegl and Tiller [30]. The global index A for the shape functions is connected to the indices $\mathrm{i}\in[1,\dots,n]$, $\mathrm{j}\in[1,\dots,m]$ and $\mathfrak{k}\in[1,\dots,l]$ in the parameter space. In particular, a connectivity array is used for implementation, similar to the location matrix defined in Hughes [22], such that the shape functions $R^{A,(i)}(\boldsymbol{\xi})$ are associated with the control points $A\in\omega^{(i)}=\{1,\dots,n^{(i)}_{\mathrm{node}}\}$, where, $n^{(i)}_{\mathrm{node}}$ denotes the total number of control points. Hence we can define a configuration vector and the variation thereof

$$\mathbf{q}^{(i)}(t)=\begin{bmatrix}\mathbf{q}_1^{(i)}(t)\\ \vdots\\ \mathbf{q}_{n^{(i)}_{\mathrm{node}}}^{(i)}(t)\end{bmatrix},\quad\delta\mathbf{q}^{(i)}(t)=\begin{bmatrix}\delta\mathbf{q}_1^{(i)}(t)\\ \vdots\\ \delta\mathbf{q}_{n^{(i)}_{\mathrm{node}}}^{(i)}(t)\end{bmatrix}. \tag{13}$$

At last, three so called knot vectors $\Xi=\{\xi_1,\xi_2,\dots,\xi_{n+p+1}\}$, $\mathcal{H}=\{\eta_1,\eta_2,\dots,\eta_{n+p+1}\}$ and $\mathcal{I}=\{\zeta_1,\zeta_2,\dots,\zeta_{n+p+1}\}$ represent a set of coordinates in the parameter space, which provide a definition for finite elements, such that a point $A:\mathrm{i,j,\mathfrak{k}}\to\xi_{\mathrm{i}},\eta_{\mathrm{j}},\zeta_{\mathfrak{k}}$ in the parameter space addresses a node in the physical space, i.e. a corner of an element.

Remark. Details on the characteristics of the isogeometric approach such as continuity, explicit representation of specific shape functions and repeated knots, mesh generation and refinement can be found in Cottrell et al. [7] and the references therein. We will deal with this specific class of shape functions in a general way, such that the following domain decomposition method can be applied without restrictions to all possible NURBS solids. Note that the control points $\mathbf{q}_A^{(i)}$ can be dealt with analogues to the nodes of Lagrangian elements. We only have to take care about the fact that the control points can be, but do not have to be part of the geometry, i.e. of the curve, surface or solid.

3.1. Discrete virtual work

Now, the semi-discrete form of the virtual work reads[2]

$$G^{\mathrm{h}}(\mathbf{q},\delta\mathbf{q})=\sum_i\delta\mathbf{q}_A^{(i)}\cdot\left[M^{AB,(i)}\ddot{\mathbf{q}}_B^{(i)}+\mathbf{f}^{(i),\mathrm{int},A}+\mathbf{f}^{(i),\mathrm{ext},A}+\mathbf{f}^{(i),d,A}\right] \tag{14}$$

where the elements of the mass matrix are

$$M^{AB,(i)}=\left\langle\rho_0R^{A,(i)},R^{B,(i)}\right\rangle^{(i)} \tag{15}$$

and the internal and external forces take the form

[2] If convenient and unique we make use of the summation convention for repeated indices.

$$\mathbf{f}^{(i),\mathrm{int},A} = \left\langle \nabla R^{A,(i)} \cdot S^{(i)}, \nabla R^{B,(i)} \right\rangle^{(i)} \mathbf{q}_B^{(i)} \tag{16}$$

and

$$\mathbf{f}^{(i),\mathrm{ext},A} = -\left\langle R^{A,(i)}, \rho_0 \bar{\mathbf{B}}^{(i)} \right\rangle^{(i)} - \left\langle R^{A,(i)}, \bar{\mathbf{T}}^{(i)} \right\rangle_{\Gamma_\sigma^{(i)}}, \tag{17}$$

respectively. The second Piola–Kirchhoff stress tensor $S^{(i)} = 2\partial W / \partial \mathbf{C}^{(i),\mathrm{h}}$ is associated with the strain energy function

$$V^{(i),\mathrm{int}}(\mathbf{q}^{(i)}) = \left\langle W(\mathbf{C}^{(i),\mathrm{h}}), 1 \right\rangle^{(i)}, \tag{18}$$

where

$$\mathbf{C}^{(i),\mathrm{h}} = \mathbf{q}_A^{(i)} \cdot \mathbf{q}_B^{(i)} \nabla R^{A,(i)} \otimes \nabla R^{B,(i)} \tag{19}$$

Note that the derivative ∇R^A can be calculated in a straightforward manner

$$\nabla R^A = (\mathbf{J}^{-1})^T \frac{\partial R^A}{\partial \boldsymbol{\xi}}, \quad \mathbf{J} = \frac{\partial \boldsymbol{\varphi}^{\mathrm{h}}}{\partial \boldsymbol{\xi}} \tag{20}$$

and $\partial R^A / \partial \boldsymbol{\xi}$ follows directly from (10). The last force contribution $\mathbf{f}^{(i),d,A}$ in (14) will be dealt with in Section 3.3.

3.2. Discrete mesh-tying constraints

The goal of this section is to provide an adequate, mortar based method for a nonconforming domain decomposition of NURBS based solids. The discrete balance of linear momentum across the interface reads

$$\left\langle \mathbf{t}^{(1),\mathrm{h}}, \left(\delta\boldsymbol{\varphi}^{(1),\mathrm{h}} - \delta\boldsymbol{\varphi}^{(2),\mathrm{h}}\right) \right\rangle_{\Gamma_d^{(1)}} = 0, \tag{21}$$

where we have to define $\mathbf{t}^{(1),\mathrm{h}}$ for NURBS based interfaces which are usually of higher order. A brief discussion of higher order (in particular quadratic) interpolation in connection with mortar contact methods can be found in Puso et al. [32] and in Fischer and Wriggers [11], a detailed analysis can be found in Hauret and Le Tallec [16]. In Hesch and Betsch [18,19] the shape functions of the underlying displacement approximation are used to interpolate the Lagrange multipliers. Optimal convergence for higher order NURBS interpolation can only be achieved by using higher order interpolation of the Lagrange multiplier field, i.e. a quadratic interpolation of the Lagrange multipliers for cubic interpolation of the geometry. Higher order NURBS interpolation of the Lagrange multiplier field may become difficult, if the interface is not constructed by an open knot vector. In that case, the interpolation of the interface depends on a large set of control points, resulting in a large number of constraints which is inefficient and potentially overconstrained. A higher order Lagrangian interpolation is possible if additional nodes are placed on the interface. Here, we restrict ourself to linear shape functions due to the generality within the application, i.e. we can apply it to arbitrary h-, p- and k-refined bodies.

Note that this approach is potentially underconstrained for extremely coarse meshes in conjunction with higher order NURBS. In general, a one dimensional system has a knot vector with $n + p + 1$ entries which correlates in our approach with the number of Lagrange multipliers reduced by the overall number of multiplicities.

Four corner nodes of each surface element of the interface, independent of the order of the underlying NURBS solid are given, such that we can always apply a linear interpolation of the Lagrange multipliers

$$\mathbf{t}^{(1),\mathrm{h}} = \sum_{A \in \tilde{\omega}^{(1)}} N^A \boldsymbol{\lambda}_A. \tag{22}$$

Here, $N^A : \mathcal{B} \to \mathbb{R}$ are linear Lagrangian shape functions associated with the nodes $A \in \tilde{\omega}^{(1)}$, where $\tilde{\omega}^{(1)}$ denotes the set of element nodes (not the control nodes) at the physical surface. Inserting (22) in (21) yields

$$\boldsymbol{\lambda}_A \cdot \left(n^{AB} \delta \mathbf{q}_B^{(1)} - n^{AC} \delta \mathbf{q}_C^{(2)} \right) = 0, \tag{23}$$

where n^{AB} and n^{AC} are the mortar integrals, given by

$$\begin{aligned} n^{AB} &= \langle N^A, R^B \rangle_{\Gamma_d^{(1)}}, \\ n^{AC} &= \langle N^A, R^C \rangle_{\Gamma_d^{(1)}}. \end{aligned} \tag{24}$$

The NURBS parametrization $\sum_B R^B \mathbf{q}_B$ and $\sum_C R^C \mathbf{q}_C$ of the respective interface surface can be derived from the adjacent volume element, as shown in Temizer et al. [33].

Remark. The presented linear interpolation of the Lagrange multipliers can be used independent of the order of the NURBS. As a result, the proposed method allows the combined use of Lagrangian and NURBS based shape functions.

3.3. Evaluation of the mortar integrals

Next a segmentation process for the numerical evaluation of the mortar integrals in (24) will be developed. To illustrate this process, we utilize a 3d version of Cook's membrane, shown in Fig. 1. For details on the geometry and the mesh see Section 5.1. The NURBS in this example are of order $p, q, r = 2$ and $5 \times 5 \times 5$ control points are used to control $3 \times 3 \times 3$ elements. Then we decompose the membrane into two nonconforming discretized parts by successively eliminating elements and applying an h-refinement to the left part, such that this part consists of $2 \times 4 \times 4$ elements. In contrast to that the right part consists of $1 \times 3 \times 3$ elements, see Fig. 2. Note that there are different ways to decompose a given CAD geometry. The geometry can be decomposed and then meshed independently, or we can mesh the whole system and decompose the mesh afterwards. Since the last one is more general and includes the former we focus on this approach.

Next, we have to split the internal surfaces into segments. Several efficient and powerful segmentation routines have been developed in the past (see [31,32,18,20]), which can be modified with little effort for NURBS based solids. To illustrate these modifications, we adapt the 4-step method in Hesch and Betsch [20]:

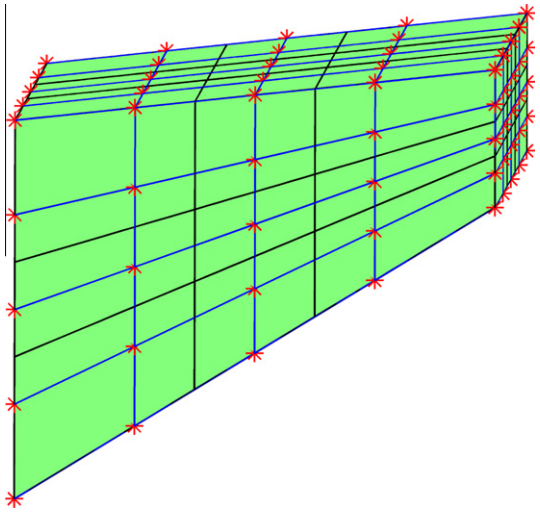

Fig. 1. Cook's membrane. The black lines indicate the mesh, while the blue lines and the red stars illustrate the control mesh and the control points respectively. (For interpretation of the references to colour in this figure legend, the reader is referred to the web version of this article.)

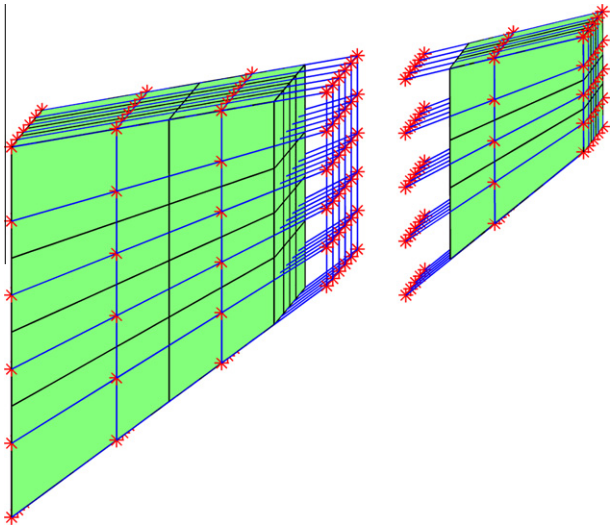

Fig. 2. Decomposed and partially refined Cook's membrane.

(1) Project orthogonally the nodes on the mortar side to the opposing surface using the KTS algorithm developed in Temizer et al. [33].
(2) Project orthogonally the nodes on the non-mortar side using once again the KTS algorithm. Note that we do not project on a projected mesh as in Hesch and Betsch [20] to simplify the algorithm.
(3) Search for intersections between the edges. The algorithm in Hesch and Betsch [20] can be adapted by using the NURBS shape functions for the edges. Similar to the surfaces the edges can be derived from the adjacent volume elements.
(4) Apply a Delaunay triangularization to each element on the mortar side. The triangularization is related to the parameter space, thus no modification is necessary.

In Fig. 3 the segmentation of the decomposed membrane is displayed. Note that the segmentation process runs independently of any application of h-, p- or k-refinements, since we always obtain surface elements with 4 corner nodes and 4 corresponding edges in the physical space.

For each segment we obtain local coordinates $\xi^{(j)}_{\text{seg},K}, K \in [1,2,3]$ in the parameter space for each surface j, defining the vertices of the segment. Introducing linear, triangular shape functions M^K a linear transformation

$$\xi^{(j),\text{h}}_{\text{seg}}(\boldsymbol{\eta}) = \sum_{K=1}^{3} M^K(\boldsymbol{\eta})\,\xi^{(j)}_{\text{seg},K}, \tag{25}$$

can be applied to parametrize the interface. The mortar integrals for each segment can now be calculated by insertion of (25) in (24). Thus, we obtain for the segment contributions

$$\begin{aligned} n^{\kappa\beta} &= \left\langle N^{\kappa}\left(\xi^{(1),\text{h}}_{\text{seg}}(\boldsymbol{\eta})\right) R^{\beta}\left(\xi^{(1),\text{h}}_{\text{seg}}(\boldsymbol{\eta})\right)\right\rangle_{\Gamma^{(1)}_{d,\text{seg}}}, \\ n^{\kappa\zeta} &= \left\langle N^{\kappa}\left(\xi^{(1),\text{h}}_{\text{seg}}(\boldsymbol{\eta})\right) R^{\zeta}\left(\xi^{(2),\text{h}}_{\text{seg}}(\boldsymbol{\eta})\right)\right\rangle_{\Gamma^{(1)}_{d,\text{seg}}}. \end{aligned} \tag{26}$$

To apply a Gauss integration, the Jacobian J_{seg} of each segment is required

$$J_{\text{seg}} = \left\| \mathbf{A}_1\left(\xi^{(1),\text{h}}_{\text{seg}}(\boldsymbol{\eta})\right) \times \mathbf{A}_2\left(\xi^{(1),\text{h}}_{\text{seg}}(\boldsymbol{\eta})\right)\right\| \det\left(D\xi(\boldsymbol{\eta})\right), \tag{27}$$

where $\mathbf{A}_\alpha(\xi) = \sum_B R^B_\alpha(\xi)\mathbf{q}_B$ denotes the tangential vectors in the reference configuration. Eventually, we obtain

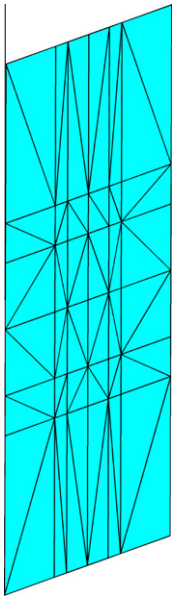

Fig. 3. Segmentation of the interface.

$$\begin{aligned} n^{\kappa\beta} &= \int_{\triangle} N^{\kappa}\left(\xi^{(1),\text{h}}_{\text{seg}}(\boldsymbol{\eta})\right) R^{\beta}\left(\xi^{(1),\text{h}}_{\text{seg}}(\boldsymbol{\eta})\right) J_{\text{seg}}\, d\eta, \\ n^{\kappa\zeta} &= \int_{\triangle} N^{\kappa}\left(\xi^{(1),\text{h}}_{\text{seg}}(\boldsymbol{\eta})\right) R^{\zeta}\left(\xi^{(2),\text{h}}_{\text{seg}}(\boldsymbol{\eta})\right) J_{\text{seg}}\, d\eta. \end{aligned} \tag{28}$$

In a last step, we collect the segment contributions

$$\boldsymbol{\Phi}^{\kappa}_{e,\text{seg}} = n^{\kappa\beta}\mathbf{q}^{(1)}_{\beta} - n^{\kappa\zeta}\mathbf{q}^{(2)}_{\zeta}, \tag{29}$$

of each element e and assemble them into a global vector of constraints

$$\boldsymbol{\Phi}(\mathbf{q}) = \mathbf{A}_{e\in\epsilon^{(1)}} \bigcup_{\text{seg}} \begin{bmatrix} \boldsymbol{\Phi}^{\kappa=1}_{e,\text{seg}} \\ \vdots \\ \boldsymbol{\Phi}^{\kappa=2}_{e,\text{seg}} \end{bmatrix}, \tag{30}$$

where $\epsilon^{(1)}$ denotes all elements on $\Gamma^{(1)}_d$. For the implementation of the assembly, a location array $A = LM(\kappa, e)$ is needed to connect the segment contributions to a specific constraint, for details see Hesch and Betsch [17]. Note that the corresponding nodal force vector $\mathbf{f}^{(i),d,A}$ follows from

$$\delta\mathbf{q}^{(i)}_A \cdot \mathbf{f}^{(i),d,A} = \delta\mathbf{q}^{(i)}_A \cdot \nabla_{\mathbf{q}_A}\boldsymbol{\Phi}(\mathbf{q}) \cdot \boldsymbol{\lambda}_A. \tag{31}$$

Remark 1. The physical position of the Gauss points on both surfaces do not necessarily coincide with their orthogonal projections, although the corner nodes of the segments do. An alternative solution relies on the evaluation of the orthogonally projected Gauss points instead of the careful evaluation of the mortar projections. More details on this discussion can be found in Puso et al. [32].

Remark 2. As shown in Puso [31], warped meshes can not be exactly integrated. Within our numerical tests, a 4 point Gauss integration has shown to be sufficient, but the number of quadrature points should be adjusted for higher order NURBS.

3.4. Reformulation of the mortar constraints

In this section we propose a reformulation of the mortar constraints following the development in Hesch and Betsch [18] to

retain conservation of both linear and angular momentum. Therefore, we decompose the Lagrange multipliers into normal and tangential components

$$\boldsymbol{\lambda} = \lambda_N \boldsymbol{n}_{\text{seg}} + \lambda^\alpha \boldsymbol{a}_{\alpha,\text{seg}}, \tag{32}$$

where

$$\boldsymbol{a}_{\alpha,\text{seg}} = \sum_A R^A_{,\alpha}\left(\xi^{(1),\text{h}}_{\text{seg}}(\bar{\boldsymbol{\eta}})\right)\mathbf{q}_A \tag{33}$$

and

$$\boldsymbol{n}_{\text{seg}} = \frac{\boldsymbol{a}_{1,\text{seg}} \times \boldsymbol{a}_{2,\text{seg}}}{\|\boldsymbol{a}_{1,\text{seg}} \times \boldsymbol{a}_{2,\text{seg}}\|} \tag{34}$$

are evaluated at the mid-point $\bar{\boldsymbol{\eta}}$ of each segment. We assume that the normal and the tangential vectors remain constant throughout each segment, simplifying the evaluation of the mortar integrals.

The reformulated segment contributions of the mortar constraints are given by

$$\bar{\boldsymbol{\Phi}}^\kappa_{e,\text{seg}} = \begin{bmatrix} \boldsymbol{\Phi}^\kappa_{e,\text{seg}} \cdot \boldsymbol{a}_1 \\ \boldsymbol{\Phi}^\kappa_{e,\text{seg}} \cdot \boldsymbol{a}_2 \\ \boldsymbol{\Phi}^\kappa_{e,\text{seg}} \cdot \boldsymbol{n} \end{bmatrix} - \bar{\boldsymbol{\Phi}}^{\kappa,\text{ref}}_{e,\text{seg}}, \tag{35}$$

where $\bar{\boldsymbol{\Phi}}^{\kappa,\text{ref}}_{e,\text{seg}}$ denotes the segment contributions of the mortar constraints evaluated in the reference configuration, computed once at problem initialization. This ensures that the constraints are fulfilled in the reference configuration. Note that if the mesh generation and refinement does not produce any gaps between the sub-domains and the position of the Gauss points on both surfaces coincide in the physical space (cf. Remark 1 in Section 3.3), then $\bar{\boldsymbol{\Phi}}^{\kappa,\text{ref}}_{e,\text{seg}} = 0$.

3.5. Augmented coordinates

Guided by the development in Hesch and Betsch [19] we introduce augmented coordinates $\boldsymbol{d}_A$ which equal the normal vector evaluated at each corner node of the elements, analogues to the Lagrange multipliers. To determine the value of the augmented coordinates, we apply additional constraints[3]

$$\boldsymbol{\Phi}^{\text{aug}} = \begin{bmatrix} \boldsymbol{d}_A \cdot \boldsymbol{a}_1 \\ \boldsymbol{d}_A \cdot \boldsymbol{a}_2 \\ \boldsymbol{d}_A \cdot \boldsymbol{d}_A - 1 \end{bmatrix} \tag{36}$$

and interpolate the augmented coordinates using the linear shape functions introduced for the interpolation of the Lagrange multipliers

$$\boldsymbol{d}_{\text{seg}} = \sum_{A \in \dot{\omega}^{(1)}} N^A(\xi^{(1),\text{h}}_{\text{seg}}(\bar{\boldsymbol{\eta}}))\boldsymbol{d}_A. \tag{37}$$

The reformulated mortar constraints can be recast by employing the augmented coordinates to obtain

$$\tilde{\boldsymbol{\Phi}}^\kappa_{e,\text{seg}} = \begin{bmatrix} \boldsymbol{\Phi}^\kappa_{e,\text{seg}} \cdot \boldsymbol{a}_1 \\ \boldsymbol{\Phi}^\kappa_{e,\text{seg}} \cdot \boldsymbol{a}_2 \\ \boldsymbol{\Phi}^\kappa_{e,\text{seg}} \cdot \boldsymbol{d}_{\text{seg}} \end{bmatrix} - \bar{\boldsymbol{\Phi}}^{\kappa,\text{ref}}_{e,\text{seg}}, \tag{38}$$

where $\bar{\boldsymbol{\Phi}}^{\kappa,\text{ref}}_{e,\text{seg}}$ remains unchanged.

3.6. Frame-indifference of the mortar constraints

For the verification of frame-indifference, we consider rigid motions of the form

$$\mathbf{q}^\sharp_A = \mathbf{c} + \mathbf{Q}\mathbf{q}_A, \tag{39}$$

where $\mathbf{c} \in \mathbb{R}^3$ and $\mathbf{Q} \in$ SO(3) is a rotation tensor. It is easy to show that one gets for the convective base vectors

$$\boldsymbol{a}^\sharp_\alpha = \mathbf{Q}\sum_A R^A_{,\alpha}\mathbf{q}_A = \mathbf{Q}\boldsymbol{a}_\alpha \tag{40}$$

and

$$\boldsymbol{n}^\sharp = \frac{\mathbf{Q}\boldsymbol{a}_1 \times \mathbf{Q}\boldsymbol{a}_2}{\|\mathbf{Q}\boldsymbol{a}_1 \times \mathbf{Q}\boldsymbol{a}_2\|} = \mathbf{Q}\boldsymbol{n}. \tag{41}$$

Thus, for the constraints (35) follows immediately

$$\bar{\boldsymbol{\Phi}}^\kappa_{e,\text{seg}}(\mathbf{q}^\sharp) = \begin{bmatrix} \boldsymbol{\Phi}^\kappa_{e,\text{seg}} \cdot \mathbf{Q}^T\mathbf{Q}\boldsymbol{a}_1 \\ \boldsymbol{\Phi}^\kappa_{e,\text{seg}} \cdot \mathbf{Q}^T\mathbf{Q}\boldsymbol{a}_2 \\ \boldsymbol{\Phi}^\kappa_{e,\text{seg}} \cdot \mathbf{Q}^T\mathbf{Q}\boldsymbol{n} \end{bmatrix} - \bar{\boldsymbol{\Phi}}^{\kappa,\text{ref}}_{e,\text{seg}} = \bar{\boldsymbol{\Phi}}^\kappa_{e,\text{seg}}(\mathbf{q}), \tag{42}$$

provided that

$$\sum_\beta n^{\kappa\beta} - \sum_\zeta n^{\kappa\zeta} = 0 \tag{43}$$

is valid (for a detailed discussion see Puso [31]). With regard to (36) and (38) it is obvious that

$$\boldsymbol{\Phi}^{\text{aug}}(\mathbf{q}^\sharp, \boldsymbol{d}) = \boldsymbol{\Phi}^{\text{aug}}(\mathbf{q}, \mathbf{Q}^T\boldsymbol{d}) \tag{44}$$

and

$$\tilde{\boldsymbol{\Phi}}^\kappa_{e,\text{seg}}(\mathbf{q}^\sharp, \boldsymbol{d}) = \tilde{\boldsymbol{\Phi}}^\kappa_{e,\text{seg}}(\mathbf{q}, \mathbf{Q}^T\boldsymbol{d}). \tag{45}$$

For later use we substitute $\mathbf{q}^A_\epsilon = \mathbf{q}^A + \epsilon\boldsymbol{\mu}$. Frame-indifference of the constraints, i.e. $\tilde{\boldsymbol{\Phi}}^\kappa_{e,\text{seg}}(\mathbf{q}_\epsilon, \boldsymbol{d}) = \tilde{\boldsymbol{\Phi}}^\kappa_{e,\text{seg}}(\mathbf{q}, \boldsymbol{d})$ implies translational invariance for arbitrary ϵ. Consequently,

$$\left.\frac{d}{d\epsilon}\right|_{\epsilon=0} \tilde{\boldsymbol{\Phi}}^\kappa_{e,\text{seg}}(\mathbf{q}_\epsilon, \boldsymbol{d}) = 0 \tag{46}$$

for any $\boldsymbol{\mu} \in \mathbb{R}^3$. Similarly, we substitute $\mathbf{q}^A_\epsilon = \exp(\epsilon\hat{\boldsymbol{\mu}})\mathbf{q}^A$, where $\exp(\hat{\boldsymbol{\mu}}) \in SO(3)$ denotes the exponential map of a skew-symmetric tensor $\hat{\boldsymbol{\mu}}$, such that $\hat{\boldsymbol{\mu}}\boldsymbol{a} = \boldsymbol{\mu} \times \boldsymbol{a}$ for arbitrary $\boldsymbol{a} \in \mathbb{R}^3$ and receive

$$\left.\frac{d}{d\epsilon}\right|_{\epsilon=0} \tilde{\boldsymbol{\Phi}}^\kappa_{e,\text{seg}}(\exp(\epsilon\hat{\boldsymbol{\mu}})\mathbf{q}, \boldsymbol{d}) - \tilde{\boldsymbol{\Phi}}^\kappa_{e,\text{seg}}(\mathbf{q}, \exp(-\epsilon\hat{\boldsymbol{\mu}})\boldsymbol{d}) = 0, \tag{47}$$

where we have made use of the rotational properties in (45). Note that the properties (46) and (47) hold for (36) as well.

4. Discretization in time

At last we deal with the discretization in time of the finite-dimensional mechanical system under consideration. To this end we cast the discrete version of (7) into the form

$$\begin{aligned} \mathbf{M}\ddot{\mathbf{q}} &= -\nabla V(\mathbf{q}) - (\mathrm{D}_1\boldsymbol{\Phi}(\mathbf{q}, \boldsymbol{d}))^T\boldsymbol{\lambda}, \\ 0 &= (\mathrm{D}_2\boldsymbol{\Phi}(\mathbf{q}, \boldsymbol{d}))^T\boldsymbol{\lambda}, \\ 0 &= \boldsymbol{\Phi}(\mathbf{q}, \boldsymbol{d}). \end{aligned} \tag{48}$$

Here the operators D_1 and D_2 denote the derivative of the vector of constraints $\boldsymbol{\Phi}(\mathbf{q}, \boldsymbol{d})$ with respect to the first and the second slot. Furthermore, $\mathbf{q}$ consists of the different sub-domain contributions of $(13)_1$ and $\mathbf{M}$ consists of the contributions $M^{AB,(i)}$ corresponding to $\delta\mathbf{q}^{(i)}_A$ and $\mathbf{q}^{(i)}_B$. Similar, $\boldsymbol{\Phi}$ and $\boldsymbol{\lambda}$ are assembled from (36) and (38) in conjunction with (30). Note that the reformulated constraints (35) can be easily implemented using approach (48) by removing the augmented coordinates and replacing the constraints. Next, we apply an energy–momentum scheme (see [18]) as follows

[3] In contrast to previous developments we can now make use of the higher continuity of the surface, such that the tangential vectors at the surface are uniquely defined.

$$\begin{aligned}
&\mathbf{q}_{n+1}-\mathbf{q}_n=\Delta t\mathbf{v}_{n+1/2},\\
&\mathbf{M}(\mathbf{v}_{n+1}-\mathbf{v}_n)=-\Delta t\bar{\nabla}V(\mathbf{q}_n,\mathbf{q}_{n+1})-\Delta t(\mathrm{D}_1\boldsymbol{\Phi}(\mathbf{q}_{n+1/2},\boldsymbol{d}_{n+1/2}))^T\boldsymbol{\lambda}_{n+1},\\
&0=(\mathrm{D}_2\boldsymbol{\Phi}(\mathbf{q}_{n+1/2},\boldsymbol{d}_{n+1/2}))^T\boldsymbol{\lambda}_{n+1},\\
&0=\boldsymbol{\Phi}(\mathbf{q}_{n+1},\boldsymbol{d}_{n+1}),
\end{aligned}\tag{49}$$

where $(\bullet)_{n+1/2}=[(\bullet)_n+(\bullet)_{n+1}]/2$ denotes the mid-point configuration for a typical time-step $n\to n+1$ using a time-step size Δt. $\bar{\nabla}V(\mathbf{q}_n,\mathbf{q}_{n+1})$ denotes the discrete gradient of the strain energy function in the sense of Gonzalez [14]. In fact, the time integration scheme is not effected by the use of NURBS based shape functions, such that we can follow the arguments in Hesch and Betsch [18] to verify the conservation properties in a brief summary.

4.1. Conservation properties

4.1.1. Conservation of linear momentum

Assuming the absence of external forces we obtain for the linear momentum map $\boldsymbol{L}$ within each time-step

$$\begin{aligned}
&\boldsymbol{\mu}\cdot(\boldsymbol{L}_{n+1}-\boldsymbol{L}_n)\\
&\quad=-\Delta t\boldsymbol{\mu}\cdot\sum_{A\in\omega}\left[\bar{\nabla}_{\mathbf{q}_A}V(\mathbf{q}_n,\mathbf{q}_{n+1})+\nabla_{\mathbf{q}_A}\boldsymbol{\Phi}(\mathbf{q}_{n+1/2},\boldsymbol{d}_{n+1/2})\boldsymbol{\lambda}_{n+1}\right].
\end{aligned}\tag{50}$$

For the first term on the right hand we receive

$$\boldsymbol{\mu}\cdot\left\langle\left(\sum_{A\in\omega}\nabla R^A\right)\cdot\boldsymbol{\Sigma}^{\mathrm{h}}_{n,n+1},\nabla R^B\right\rangle\mathbf{q}_{B,n+1/2}=0.\tag{51}$$

Note that the discrete second Piola–Kirchhoff stress tensor reads

$$\begin{aligned}
\boldsymbol{\Sigma}^{\mathrm{h}}_{n,n+1}=&2\mathrm{D}W(\boldsymbol{C}^{\mathrm{h}}_{n+1/2})\\
&+\frac{W\left(\boldsymbol{C}^{\mathrm{h}}_{n+1}\right)-W\left(\boldsymbol{C}^{\mathrm{h}}_{n}\right)-\mathrm{D}W\left(\boldsymbol{C}^{\mathrm{h}}_{n+1/2}\right):\left[\boldsymbol{C}^{\mathrm{h}}_{n+1}-\boldsymbol{C}^{\mathrm{h}}_{n}\right]}{\left\|\boldsymbol{C}^{\mathrm{h}}_{n+1}-\boldsymbol{C}^{\mathrm{h}}_{n}\right\|^2}\left[\boldsymbol{C}^{\mathrm{h}}_{n+1}-\boldsymbol{C}^{\mathrm{h}}_{n}\right].
\end{aligned}\tag{52}$$

For the second term follows

$$-\Delta t\boldsymbol{\mu}\cdot\sum_{A\in\omega}\nabla_{\mathbf{q}_A}\boldsymbol{\Phi}(\mathbf{q}_{n+1/2},\boldsymbol{d}_{n+1/2})\boldsymbol{\lambda}_{n+1}=0,\tag{53}$$

where we have made use of property (46).

4.1.2. Conservation of angular momentum

For the angular momentum map $\boldsymbol{J}$ follows analogously

$$\begin{aligned}
\boldsymbol{\mu}\cdot(\boldsymbol{J}_{n+1}-\boldsymbol{J}_n)=&-\Delta t\sum_{A\in\omega}\mathbf{q}_{A,n+1/2}\\
&\times\left[\bar{\nabla}_{\mathbf{q}_A}V(\mathbf{q}_n,\mathbf{q}_{n+1})+\nabla_{\mathbf{q}_A}\boldsymbol{\Phi}(\mathbf{q}_{n+1/2},\boldsymbol{d}_{n+1/2})\boldsymbol{\lambda}_{n+1}\right].
\end{aligned}\tag{54}$$

The first term vanishes due to the skew-symmetry of $\mathbf{q}_{A,n+1/2}\times\mathbf{q}_{B,n+1/2}$ and the symmetry of $\boldsymbol{\Sigma}^{\mathrm{h}}_{n,n+1}$. For the second term follows

$$\begin{aligned}
\boldsymbol{\mu}\cdot(\boldsymbol{J}_{n+1}-\boldsymbol{J}_n)&=-\Delta t\sum_{A\in\omega}\mathbf{q}_{A,n+1/2}\times\nabla_{\mathbf{q}_A}\boldsymbol{\Phi}(\mathbf{q}_{n+1/2},\boldsymbol{d}_{n+1/2})\boldsymbol{\lambda}_{n+1}\\
&=\Delta t\boldsymbol{\lambda}_{n+1}\cdot\sum_{A\in\omega}(\nabla_{\mathbf{q}_A}\boldsymbol{\Phi}(\mathbf{q}_{n+1/2},\boldsymbol{d}_{n+1/2}))^T\hat{\mathbf{q}}_{A,n+1/2}\boldsymbol{\mu}\\
&=-\Delta t\boldsymbol{\lambda}_{n+1}\cdot\sum_{A\in\omega^{(1)}}(\nabla_{\boldsymbol{d}_A}\boldsymbol{\Phi}(\mathbf{q}_{n+1/2},\boldsymbol{d}_{n+1/2}))^T\hat{d}_{A,n+1/2}\boldsymbol{\mu}\\
&=\Delta t\boldsymbol{\mu}\cdot\sum_{A\in\omega^{(1)}}\hat{d}_{A,n+1/2}\nabla_{\boldsymbol{d}_A}\boldsymbol{\Phi}(\mathbf{q}_{n+1/2},\boldsymbol{d}_{n+1/2})\boldsymbol{\lambda}_{n+1}=0,
\end{aligned}\tag{55}$$

where we have taken (47) and $(49)_3$ into account.

4.1.3. Conservation of energy

Eventually, we verify algorithmic conservation of energy. Scalar multiplication of $(49)_2$ by $\mathbf{v}_{n+1/2}$ yields

$$\begin{aligned}
\mathbf{v}_{n+1/2}\cdot\mathbf{M}(\mathbf{v}_{n+1}-\mathbf{v}_n)=&-(\mathbf{q}_{n+1}-\mathbf{q}_n)\cdot\bar{\nabla}V(\mathbf{q}_n,\mathbf{q}_{n+1})+(\mathbf{q}_{n+1}\\
&-\mathbf{q}_n)\cdot(\mathrm{D}_1\boldsymbol{\Phi}(\mathbf{q}_{n+1/2},\boldsymbol{d}_{n+1/2}))^T\boldsymbol{\lambda}_{n+1},
\end{aligned}\tag{56}$$

where we have taken $(49)_1$ into account. Due to the discrete gradient (52) we can recast the last equation as follows

$$\begin{aligned}
\frac{1}{2}\mathbf{v}_{n+1}\cdot\mathbf{M}\mathbf{v}_{n+1}-\frac{1}{2}\mathbf{v}_n\cdot\mathbf{M}\mathbf{v}_n=&-(V(\mathbf{q}_{n+1})-V(\mathbf{q}_n))+\boldsymbol{\lambda}_{n+1}\\
&\cdot\mathrm{D}_1\boldsymbol{\Phi}(\mathbf{q}_{n+1/2},\boldsymbol{d}_{n+1/2})(\mathbf{q}_{n+1}-\mathbf{q}_n).
\end{aligned}\tag{57}$$

For the last term we state that

$$\begin{aligned}
&\mathrm{D}_1\boldsymbol{\Phi}(\mathbf{q}_{n+1/2},\boldsymbol{d}_{n+1/2})(\mathbf{q}_{n+1}-\mathbf{q}_n)+\mathrm{D}_2\boldsymbol{\Phi}(\mathbf{q}_{n+1/2},\boldsymbol{d}_{n+1/2})(\boldsymbol{d}_{n+1}-\boldsymbol{d}_n)\\
&\quad=\boldsymbol{\Phi}(\mathbf{q}_{n+1},\boldsymbol{d}_{n+1})-\boldsymbol{\Phi}(\mathbf{q}_n,\boldsymbol{d}_n)=0
\end{aligned}\tag{58}$$

is valid, since the constraints are at most quadratic in $\mathbf{q}$ and $\boldsymbol{d}$ and we end up with

$$E(\mathbf{q}_{n+1},\boldsymbol{d}_{n+1})-E(\mathbf{q}_n,\boldsymbol{d}_n)=-\boldsymbol{\lambda}_{n+1}\cdot\mathrm{D}_2\boldsymbol{\Phi}(\mathbf{q}_{n+1/2},\boldsymbol{d}_{n+1/2})(\boldsymbol{d}_{n+1}-\boldsymbol{d}_n)=0,\tag{59}$$

where $E=1/2\mathbf{v}\cdot\mathbf{M}\mathbf{v}+V(\mathbf{q})$ denotes the total energy.

5. Examples

5.1. Cook's membrane

The first static example deals with a decomposed and partially h-refined membrane structure, known as Cook's membrane. In particular we consider a 3d version of Cook's membrane with constant thickness $h=10$. The initial mesh is shown in Fig. 1 consisting of $3\times3\times3$ quadratic elements whereas Fig. 2 shows the decomposed and refined mesh. The left part consists of $2\times4\times4$ and the right of $1\times3\times3$ quadratic elements. The $4\times6\times6$ and $3\times5\times5$ control points of the sub-domains are equidistant distributed to simplify mesh generation. The knot vectors are

$$\begin{aligned}
&\Xi^{(1)}=[0,0,0,1,2,3,3],\\
&\mathcal{H}^{(1)}=[0,0,0,1,2,3,4,4,4],\\
&\mathcal{I}^{(1)}=[0,0,0,1,2,3,4,4,4],\\
&\Xi^{(2)}=[0,1,2,3,3,3],\\
&\mathcal{H}^{(2)}=[0,0,0,1,2,3,3,3],\\
&\mathcal{I}^{(2)}=[0,0,0,1,2,3,3,3].
\end{aligned}\tag{60}$$

Here, the upper index refers to the left (1) and to the right (2) sub-domain. A compressible Neo-Hooke material model is applied with the strain energy function

$$W(\boldsymbol{C})=\frac{\mu}{2}[\mathrm{tr}(\boldsymbol{C})-3]+\frac{\lambda}{2}(\ln(J))^2-\mu\ln(J),\tag{61}$$

where $\mathbf{J}=\sqrt{\det(\boldsymbol{C})}$ and $\mu=865.3846$, $\lambda=1298.1$ are the corresponding Lamé parameters. A Dirichlet boundary condition has been applied to the left side, whereas a Neumann boundary condition has been applied to the right side of the membrane. In particular, a surface load acts with a constant load $P=[0,-200,500]$ on the specified surface. Fig. 4 displays the deformed configuration, whereas Fig. 5 shows the distribution of the norm of the Cauchy stresses of the left sub-domain. For comparison we have modified the KTS method (see Temizer et al. [33][4]) using Lagrange multipliers instead of a penalty method and applied it to the problem at hand. The stress distribution of the left sub-domain is displayed in Fig. 6.

[4] The KTS method relies on an pointwise enforcement of the constraints.

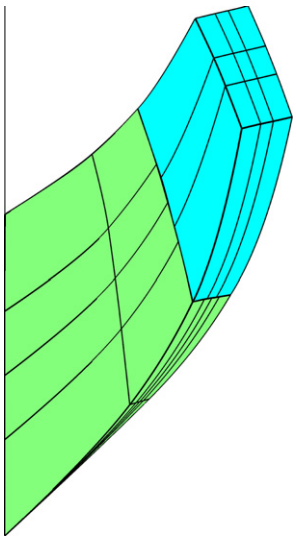

Fig. 4. Deformed configuration of the membrane.

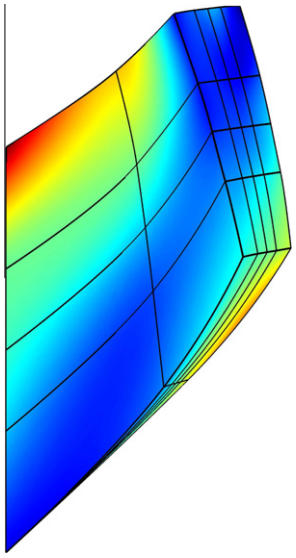

Fig. 5. Deformed configuration and stress distribution of the left sub-domain (mortar method).

Note that we have applied the Lagrange multipliers on the interface of the right sub-domain, such that we used 3×16 multipliers for the KTS as well as for the mortar method.

5.2. Patch test

The next static examples deals with a standard three dimensional patch test. An exploded drawing of the reference configuration is given in Fig. 7. The lower block is meshed using $(2 \times 2 \times 2)$ quadratic NURBS based elements, whereas the upper block is meshed using $3 \times 3 \times 3$ linear Lagrangian elements. The lower block is fixed at the bottom, such that it can elongate in the x- and y-direction, but is fixed in the z-direction, i.e. we should get a uniform and homogeneous stress distribution. A constant pressure field $P = [0, 0, -12000]$ is applied to the top of the upper block. The material model and data are the same as in Section 5.1. Fig. 8 shows the von Mises stress distribution after the application of the load to the upper body. The Lagrange multipliers are assigned to

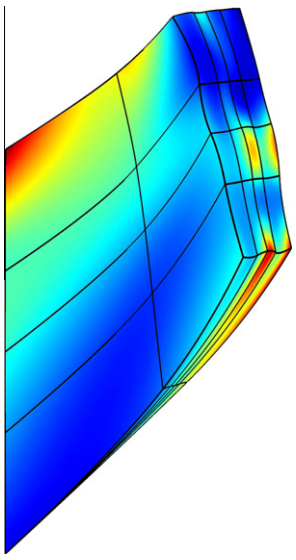

Fig. 6. Deformed configuration and stress distribution of the left sub-domain (KTS method).

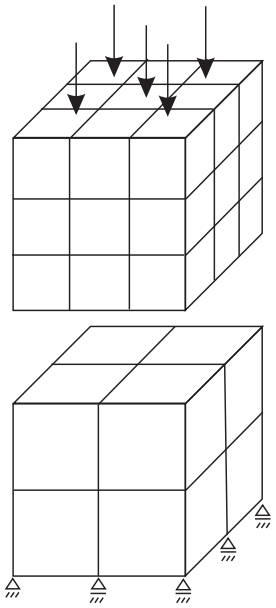

Fig. 7. Initial configuration for the patch test.

the top surface, such that we deal with 3×16 multipliers. The interface remains flat as expected.

5.3. L-shaped block

The last problem under consideration deals with an L-shaped block, decomposed into two parts as shown in Fig. 9. The larger part consists of $3 \times 3 \times 11$ quadratic NURBS based elements, the smaller part of $2 \times 2 \times 2$ quadratic NURBS based elements using overall 389 control points. An Ogden type material model

$$W(\boldsymbol{C}) = \kappa\beta^{-2}(\beta \ln(\mathbf{J}) + \mathbf{J}^{-\beta} - 1) + \sum_a \sum_p \frac{\mu_p}{\alpha_p}(\bar{\lambda}_a^{\alpha_p} - 1) \tag{62}$$

has been applied, where $\bar{\lambda}_a = J^{-1/3}\lambda_a$ are modified principal stretches. The corresponding material constants are

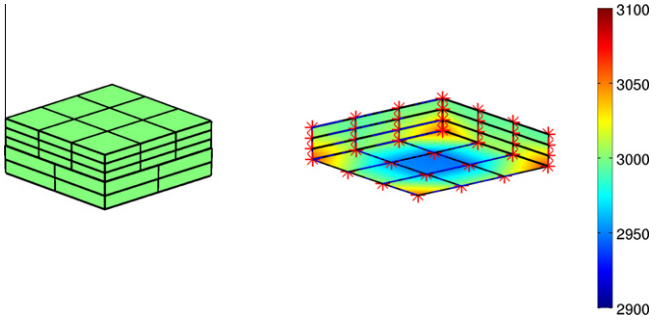

Fig. 8. Deformed configuration and stress distribution at the interface.

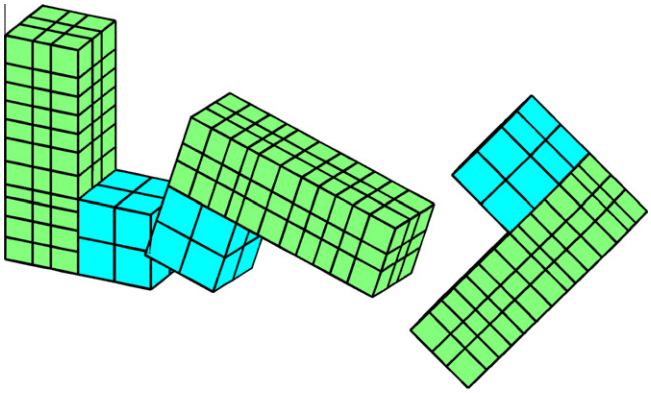

Fig. 10. Snapshots of the motion at time $t \in \{0, 10, 20\}$.

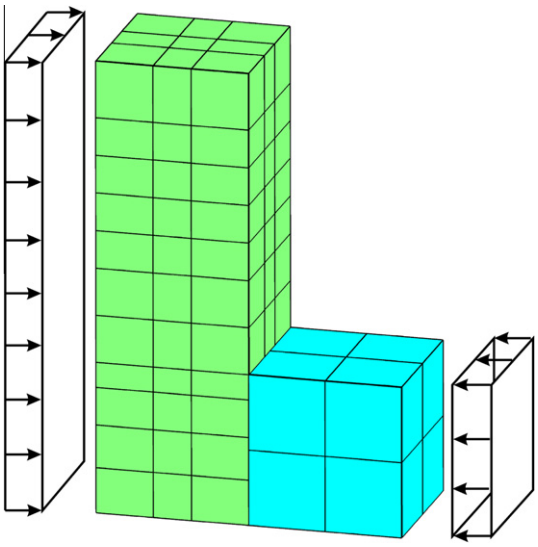

Fig. 9. Initial configuration of the L-shaped block.

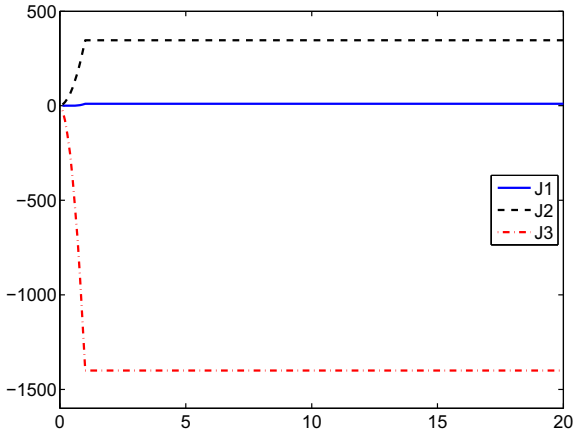

Fig. 11. Total angular momentum over time.

$$
\begin{aligned}
&\rho_0 = 10,\\
&\mu = [6.3 \cdot 10^5, 0.012 \cdot 10^5, -0.1 \cdot 10^5],\\
&\alpha = [1.3, 5.0, -2.0],\\
&\beta = 9,\\
&\kappa = 2 \cdot 10^5,
\end{aligned}
\tag{63}
$$

where ρ_0 denotes the reference density. Furthermore, 40 mortar segments and 60 Lagrange multipliers are used to enforce the mesh-tying constraints. A sinusoidal normal pressure load has been applied for the first second to the back and the front surface with $P_{\max} = 1000$. Apart from that, no other boundary conditions or external fields have been applied, such that the L-shape can move free in space. The whole time interval is set to [0,20] using a constant time-step size of $\Delta t = 0.1$. Snapshots at successive points in time are depicted in Fig. 10. The three components of angular momentum plotted over time are shown in Fig. 11. As can be seen, all three components are preserved after the initial loading phase. Furthermore, Fig. 12 shows the total energy also plotted over time. As expected, the total energy remains conserved after the initial loading phase, i.e. the change in total energy remains below the stop criterion of the Newton iteration 10^{-4}.

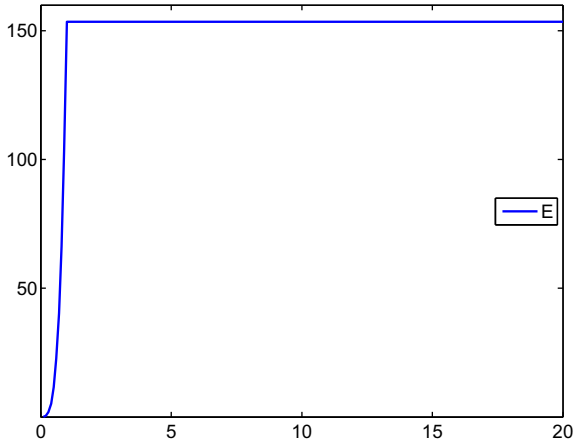

Fig. 12. Total energy over time.

6. Conclusions

In this work, we presented a newly designed mortar method for domain decomposition problems in the context of isogeometric analysis. To this end, we have redesigned the mortar integrals for the application of NURBS based shape functions. An important feature of the proposed approach is the combined use of Lagrangian and NURBS shape functions. This makes possible to apply isogeometric analysis in a reasonable fashion and to use Lagrangian shape functions if necessary.

Guided by previous developments in Hesch and Betsch [18] we have applied a specific augmentation technique to achieve an energy–momentum consistent formulation of the constrained

mechanical system at hand. In particular, the presented approach can be viewed as a straightforward extension of energy–momentum schemes to isogeometric analysis, leading to a remarkably stable and robust time integration scheme.

References

[1] O.B. Widlund, D.E. Keyes (Eds.), Domain Decomposition Methods in Science and Engineering XVI, Lecture Notes in Computational Science and Engineering, vol. 55, Springer-Verlag, 2006.

[2] Y. Bazilevs, C. Michler, V.M. Calo, T.J.R. Hughes, Weak Dirichlet boundary conditions for wall-bounded turbulent flows, Comput. Methods Appl. Mech. Engrg. 196 (2007) 4853–4862.

[3] D.J. Benson, Y. Bazilevs, M.C. Hsu, T.J.R. Hughes, Isogeometric shell analysis: The Reissner–Mindlin shell, Comput. Methods Appl. Mech. Engrg. 199 (2010) 276–289.

[4] C. Bernardi, Y. Mayday, A.T. Patera, A new nonconforming approach to domain decomposition: the mortar element method, Nonlinear Partial Differ. Eqn. Appl. (1994) 13–51.

[5] P. Betsch, P. Steinmann, Conserving properties of a time FE method – part II: time-stepping schemes for non-linear elastodynamics, Int. J. Numer. Methods Engrg. 50 (2001) 1931–1955.

[6] V. Chawla, T.A. Laursen, Energy consistent algorithms for frictional contact problems, Int. J. Numer. Methods Engrg. 42 (1998) 799–827.

[7] J.A. Cottrell, T.J.R. Hughes, Y. Bazilevs, Isogeometric Analysis: Toward Integration of CAD and FEA, Wiley, New York, 2009.

[8] J.A. Cottrell, T.J.R. Hughes, A. Reali, Studies of refinement and continuity in isogeometric structural analysis, Comput. Methods Appl. Mech. Engrg. 196 (2007) 4160–4183.

[9] J.A. Cottrell, A. Reali, Y. Bazilevs, T.J.R. Hughes, Isogeometric analysis of structural vibrations, Comput. Methods Appl. Mech. Engrg. 195 (2006) 5257–5296.

[10] T. Elguedj, Y. Bazilevs, V.M. Calo, T.J.R. Hughes, $\bar{B}$ and $\bar{F}$ projection methods for nearly incompressible linear and non-linear elasticity and plasticity using higher-order NURBS elements, Comput. Methods Appl. Mech. Engrg. (197) (2008) 2732–2762.

[11] K.A. Fischer, P. Wriggers, Mortar based frictional contact formulations for higher order interpolations using the moving friction cone, Comput. Methods Appl. Mech. Engrg. 195 (2006) 5020–5036.

[12] B. Flemisch, M.A. Puso, B.I. Wohlmuth, A new dual mortar method for curved interfaces: 2d elasticity, Int. J. Numer. Methods Engrg. 63 (2005) 813–832.

[13] H. Gomez, V.M. Calo, Y. Bazilevs, T.J.R. Hughes, Isogeometric analysis of the Cahn–Hilliard phase-field model, Comput. Methods Appl. Mech. Engrg. 197 (2008) 4333–4352.

[14] O. Gonzalez, Time integration and discrete Hamiltonian systems, J. Nonlinear Sci. 6 (1996) 449–467.

[15] P. Hauret, P. LeTallec, Energy-controlling time integration methods for nonlinear elastodynamics and low-velocity impact, Comput. Methods Appl. Mech. Engrg. 195 (2006) 4890–4916.

[16] P. Hauret, P. LeTallec, A discontinous stabilized mortar method for general 3D elastic problems, Comput. Methods Appl. Mech. Engrg. 196 (2007) 4881–4900.

[17] C. Hesch, P. Betsch, A mortar method for energy-momentum conserving schemes in frictionless dynamic contact problems, Int. J. Numer. Methods Engrg. 77 (2009) 1468–1500.

[18] C. Hesch, P. Betsch, Transient 3D domain decomposition problems: frame-indifferent mortar constraints and conserving integration, Int. J. Numer. Methods Engrg. 82 (2010) 329–358.

[19] C. Hesch, P. Betsch, Energy-momentum consistent algorithms for dynamic thermomechanical problems – application to mortar domain decomposition problems, Int. J. Numer. Methods Engrg. 86 (2011) 1277–1302.

[20] C. Hesch, P. Betsch, Transient 3d contact problems – mortar method: mixed methods and conserving integration, Computational Mechanics (2011), doi:10.1007/s00466-011-0583-8.

[21] C. Hesch, P. Betsch, Transient 3d contact problems – NTS method: mixed methods and conserving integration, Computational Mechanics (2011), doi:10.1007/s00466-011-0597-2.

[22] T.J.R. Hughes, The Finite Element Method, Dover Publications, 2000.

[23] T.J.R. Hughes, J.A. Cottrell, Y. Bazilevs, Isogeometric analysis: CAD, finite elements, NURBS, exact geometry and mesh refinement, Comput. Methods Appl. Mech. Engrg. 194 (2005) 4135–4195.

[24] M. Krüger, M. Groß, P. Betsch, A comparison of structure-preserving integrators for discrete thermoelastic systems, Comput. Mech. 47 (6) (2011) 701–722.

[25] T.A. Laursen, Computational Contact and Impact Mechanics, Springer-Verlag, 2002.

[26] T.A. Laursen, V. Chawla, Design of energy conserving algorithms for frictionless dynamic contact problems, Int. J. Numer. Methods Engrg. 40 (1997) 863–886.

[27] T.A. Laursen, G.R. Love, Improved implicit integrators for transient impact problems – geometric admissibility within the conserving framework, Int. J. Numer. Methods Engrg. 53 (2002) 245–274.

[28] S. Lipton, J.A. Evans, Y. Bazilevs, T. Elguedj, T.J.R. Hughes, Robustness of isogeometric structural discretizations under severe mesh distortion, Comput. Methods Appl. Mech. Engrg. 199 (2010) 357–373.

[29] L.D. Lorenzis, I. Temizer, P. Wriggers, G. Zavarise, A large deformation frictional contact formulation using NURBS-based isogeometric analysis, Int. J. Numer. Methods Engrg. (2011), doi:10.1002/nme.3159.

[30] L. Piegl, W. Tiller, The NURBS Book, second ed., Springer, 2010.

[31] M.A. Puso, A 3D mortar method for solid mechanics, Int. J. Numer. Methods Engrg. 59 (2004) 315–336.

[32] M.A. Puso, T.A. Laursen, J.M. Solberg, A segment-to-segment mortar contact method for quadratic elements and large deformations, Comput. Methods Appl. Mech. Engrg. 197 (2008) 555–566.

[33] I. Temizer, P. Wriggers, T.J.R. Hughes, Contact treatment in isogeometric analysis with NURBS, Comput. Methods Appl. Mech. Engrg. 200 (2011) 1100–1112.

[34] B.I. Wohlmuth, A mortar finite element method using dual spaces for the Lagrange multiplier, SIAM J. Numer. Anal. 38 (3) (2000) 989–1012.

[35] B.I. Wohlmuth, R. Krause, A multigrid method based on the unconstrained product space arising form motar finite element discretizations, SIAM J. Numer. Anal. 39 (1) (2001) 192–213.